
Research Article

Santanu Poddar and Pengfei Huo*

Quantum Dynamics Simulations of Polariton Transport in a Bloch Surface Wave Cavity

Abstract: Coupling excitons to quantized cavity photonic modes can significantly enhance the spatial and temporal range of excitonic transport. While the precise mechanism behind this dramatic change remains an active area of research, there is a growing consensus that the formation of hybrid light-matter states, known as polaritons, plays a central role in this enhancement. Polaritons, owing to their photonic character, can greatly amplify coherent energy flow in excitonic systems and prolong their lifetime and lead to ultrafast ballistic excitonic transport which is typically diffusive outside a cavity. In Bloch surface wave (BSW) cavities, the group velocity of these polaritonic wavepackets has been theoretically predicted to approach the speed of light in the medium, though experiments suggest a renormalized value.

In this work, we use quantum dynamics simulations with theoretical analysis on group velocity renormalization and wavepacket evolution to elucidate the transport dynamics in a Bloch Surface Wave Cavity. We show that polaritonic states facilitate ballistic flow directly through their photonic character, and that below a critical photonic fraction the ballistic component is suppressed—yet even then, transport remains four to eight orders of magnitude faster than purely excitonic diffusion. These results show qualitative, and in some cases near-quantitative, agreement with experimental trends, providing microscopic insight into the origin of fast transport in BSW polariton systems.

Keywords: Exciton-Polariton Transport; BSW Cavity; Photonic Crystal; Ballistic-Diffusive Transport

1 Introduction

Excitonic transport plays a central role in diverse natural and engineered systems [1–3], serving as a fundamental mechanism for energy transfer. From light harvesting in photosynthetic complexes to charge separation in optoelectronic devices [4] such as LEDs and solar cells [5, 6], the overall efficiency often hinges on the effectiveness of exciton migration. In Frenkel excitonic systems, transport typically proceeds via random hopping between localized sites—a consequence of structural and energetic disorder, thermal fluctuations, phonon interactions, and weak intermolecular electronic couplings [3, 7, 8]. Consequently, exciton motion is predominantly diffusive or subdiffusive [3, 7–9], which severely limits rapid, long-range energy transfer and constrains the performance of next-generation organic optoelectronic materials.

Recent experimental [10–19] and theoretical advances [13, 20–22] have revealed that excitonic transport can be dramatically enhanced when molecular or hybrid materials are strongly coupled to confined photonic modes, forming light–matter hybrid quasiparticles known as polaritons. Cavity-enhanced transport and other coherent phenomena in exciton–polariton systems [23] demonstrate that strong light-matter coupling can induce coherent, long-range energy migration over macroscopic distances. Remarkably, ultrafast and ballistic excitonic transport has been observed in disordered organic semiconductors [10] and perovskite metasurfaces [16, 24], even at room temperature. Similar enhancements have been reported in systems coupled to surface lattice resonances [17, 25, 26] and Bloch surface waves (BSWs) [10, 15, 27, 28]. These findings suggest that light–matter hybridization offers a powerful route to overcome diffusive exciton motion and achieve macroscopic range for energy flow. The enhanced polariton transport behavior has also been observed in other related systems [14, 29]. Persistent coherence and long-range energy propagation have been demonstrated across diverse platforms—from multilayer heterostructures [30–32] to large-area 2D semi-

Santanu Poddar, Department of Chemistry, University of Rochester, 120 Trustee Road, Rochester, New York 14627, USA; spoddar3@ur.rochester.edu;

***Corresponding author:** **Pengfei Huo**, Department of Chemistry, University of Rochester, 120 Trustee Road, Rochester, New York 14627, USA; The Institute of Optics, Hajim School of Engineering, University of Rochester, Rochester, New York 14627, USA; pengfei.huo@rochester.edu; 0000-0002-8639-9299



conductors [33]. Recent studies even indicate that organic semiconductors can sustain microcavity-like exciton–polaritons under ambient conditions without an external cavity [34]. In addition to enabling coherent transport, polaritonic systems have revealed a wealth of new phenomena, including polariton condensation [35, 36], superfluidity [37], quantized vortices [38], and the modification of chemical reaction pathways via vibrational strong coupling [39–42].

When N excitonic modes couple to \mathcal{M} photonic modes, the system forms \mathcal{M} upper polaritons (UPs), \mathcal{M} lower polaritons (LPs), and $N - \mathcal{M}$ excitonic dark states. Due to their partial photonic nature, polaritons are far more delocalized than bare excitons and can propagate coherently over hundreds of micrometers [33]. Even polaritons with high excitonic fractions (up to 80%) exhibit long-range ballistic motion [13, 24], highlighting the robustness of polariton-enabled long-range energy transport. Moreover, the delocalization of collective dark states—governed by excitonic disorder and cavity Q -factor—can significantly influence polariton velocities and overall transport efficiency [20, 21].

Theoretical and molecular quantum dynamics studies [13, 20, 22, 43, 44] indicate that enhanced transport primarily originates from the photonic component of polaritons, which promotes delocalization and sustains coherence between spatial excitonic sites, while elastic and inelastic scattering from static and dynamic disorder [21, 28, 45] suppresses ballistic motion through the excitonic channel. Static energetic disorder accounts for only a minor fraction of velocity renormalization, with dynamic (phonon-assisted) disorder dominating at moderate temperatures [28, 45]. Nevertheless, long-range coherence can persist despite such scattering [32, 43], aided by delocalization through the photonic field [14, 29]. Additionally, exciton–exciton interactions can counteract phonon-induced decoherence, stabilizing coherent transport [46, 47].

Recent advances in nanophotonics have enabled photonic architectures that support multiple exciton–polariton (EP) platforms—from Fabry–Pérot microcavities and metal–dielectric plasmonic interfaces to Bloch surface wave polaritons (BSWPs) in dielectric photonic crystals. Each platform offers distinct advantages and constraints for coherent energy transfer. In Fabry–Pérot cavities, strong coupling occurs between excitons and cavity photon modes confined between two mirrors—metallic or dielectric distributed Bragg reflectors (DBRs). Although theoretical group velocities from LP dispersion slopes can reach tens of $\mu\text{m}\cdot\text{ps}^{-1}$, experimentally measured values are typically

lower ($1\text{--}2\ \mu\text{m}\cdot\text{ps}^{-1}$) [18, 48] than the theoretical value taken from the derivative of the dispersion curve. This renormalization of polaritonic group velocity arises mainly from exciton–phonon interactions and static or dynamic disorder [21, 43, 49]. A superexchange-like mechanism between polaritonic and dark excitonic states has been proposed to explain this group velocity renormalization [49]. In addition, cavity photon loss—particularly in metallic systems—diminishes coherence and shifts transport from ballistic to diffusive [20, 21]. As the excitonic fraction increases, this diffusive transition becomes more pronounced, often erasing the ballistic character entirely.

BSW-polaritons (BSWPs) form at the interface of a homogeneous dielectric and a periodic dielectric structure, supported by a single DBR stack. These Bloch surface waves exhibit low-loss, evanescent propagation with nearly linear dispersion near $k = 0$, enabling significantly higher group velocities than Fabry–Pérot or surface plasmon polariton (SPP) systems [10, 15, 27]. Without metallic components, BSWPs experience much lower photonic dissipation, achieving propagation speeds of $10^7\text{--}10^8\ \text{m}\cdot\text{s}^{-1}$ [10, 15, 27], at least an order of magnitude higher than planar cavity or SPP systems ($\sim 10^6\ \text{m}\cdot\text{s}^{-1}$ [17]). Even polaritonic states with high excitonic content (40%) can maintain ballistic propagation. When transport becomes diffusive, BSWPs still exhibit diffusion constants [15] two orders of magnitude larger than their plasmonic counterparts [17]. These characteristics make BSWPs a uniquely promising platform for studying exciton–polariton transport and its fundamental mechanisms.

In this work, we aim to elucidate the transport dynamics of BSWP systems through quantum dynamics simulations with theoretical analysis on group velocity renormalization and wavepacket evolution. Specifically, we investigate how the spatial width of an excitonic wavepacket evolves when matter are coupled to BSWs under varying initial conditions. Using a mean-field Ehrenfest approach, we simulate the propagation of lower polariton (LP) wavepackets with tunable energy composition and extract group velocities and transport exponents as functions of photonic fraction. Our theoretical simulations reproduces the basic trends of the experimental findings in Ref. 15, with dynamical details that clarify the mechanisms governing ballistic-to-diffusive transport transitions. The results show near-quantitative agreement with experimental trends and provide valuable insights into the microscopic origin of ballistic transport in BSWP systems.

2 Theory

2.1 Hamiltonian

We consider a system composed of a one-dimensional lattice of Frenkel excitons coupled to a BSW cavity. The states $|g_n\rangle$ and $|e_n\rangle$ represent the ground and excited states at the n_{th} site, respectively. The global excitonic ground state is given by $|G\rangle = \bigotimes_n |g_n\rangle$, and the N possible singly excited states are denoted by $\{|E_n\rangle = |e_n\rangle \bigotimes_{s \neq n} |g_s\rangle\}$. The excitonic system is modeled using the tight-binding approximation, while the light-matter interaction is described using a generalized Tavis–Cummings model [13, 50–53]. Each exciton is locally coupled to a phonon bath via a Holstein-type interaction [54].

The full Hamiltonian of our system, referred to as the generalized Holstein–Tavis–Cummings (GHTC) Hamiltonian, is given by

$$\hat{H} = \sum_{n=0}^{N-1} \hbar\omega_0 \hat{\sigma}_n^\dagger \hat{\sigma}_n + \hbar \sum_k \omega_k \hat{a}_k^\dagger \hat{a}_k + \hat{H}_{\text{ex-b}} + \hat{H}_{\text{b}} \quad (1)$$

$$+ \hbar g_c \sum_{k,n} (\hat{a}_k^\dagger \hat{\sigma}_n e^{-ikx_n} + \hat{\sigma}_n^\dagger \hat{a}_k e^{ikx_n}),$$

where $\hat{\sigma}_n^\dagger$ and $\hat{\sigma}_n$ are the creation and annihilation operators for an exciton at the n_{th} site, defined as $\hat{\sigma}_n = |g_n\rangle \langle e_n|$. The excitation energy $\hbar\omega_0$ is identical at all N sites. Further, $\hbar\omega_k$ is the energy of the photonic mode with the in-plane component of wave vector k (parallel to the plane of the Bloch surface wave propagation, commonly referred to as k_{\parallel} , and is considered as the x -direction).

The operators \hat{a}_k^\dagger and \hat{a}_k are the creation and annihilation operators for the k_{th} mode, with $\hat{a}_k = |0_k\rangle \langle 1_k|$, where $|0_k\rangle$ and $|1_k\rangle$ denote the vacuum and single-photon Fock states, respectively, within the single excitation subspace as we considered in the transport dynamics. Here, we consider the BSW cavity that has a dispersion relation as follows

$$\omega_k = \omega_c + \left(\frac{c}{n_r} \right) |k|, \quad (2)$$

where c is the speed of light, n_r is the refractive index of the medium, and $|k|$ is the magnitude of the in-plane component of the photonic wave vector. The constant energy shift $\hbar\omega_c$ corresponds to the perpendicular (y -direction) component of the wave vector (the k_{\perp} component), which is the same for all modes.

The second line of Eq. 1 is the generalized Tavis–Cummings term describing the exciton-photon

interaction, with explicitly assuming the rotating wave approximation (that ignores counter rotating wave terms $\hat{a}_k^\dagger \hat{\sigma}_n^\dagger$ and, $\hat{a}_k \hat{\sigma}_n$). Further, x_n is the center of the n_{th} site, where $x_n = nL$. We impose periodic boundary conditions on the lattice, identifying the N_{th} site with the 0_{th} site. The parameter g_c denotes the single-molecule light–matter coupling strength, which is assumed to be independent of the photonic wave vector k .

The phonon vibrations (bath) have a Hamiltonian with the following form

$$\hat{H}_{\text{b}} = \sum_{n,v} \hbar\omega_v \left(\hat{b}_{n,v}^\dagger \hat{b}_{n,v} + \frac{1}{2} \right) = \sum_{n,v} \left(\frac{\hat{p}_{n,v}^2}{2} + \frac{1}{2} \omega_v^2 \hat{q}_{n,v}^2 \right), \quad (3)$$

where $\hat{b}_{n,v}^\dagger$ and $\hat{b}_{n,v}$ are the creation and annihilation operators for the v_{th} phonon mode associated with the n_{th} site, with vibrational frequency ω_v . The corresponding position and momentum operators are $\hat{q}_{n,v}$ and $\hat{p}_{n,v}$, and all phonons are assumed to have the normalized mass. The exciton-phonon interaction Hamiltonian is

$$\hat{H}_{\text{ex-b}} = \sum_{n,v} d_v \hat{\sigma}_n^\dagger \hat{\sigma}_n (\hat{b}_{n,v}^\dagger + \hat{b}_{n,v}) = \sum_{n,v} \gamma_v \hat{\sigma}_n^\dagger \hat{\sigma}_n \hat{b}_{n,v}, \quad (4)$$

where γ_v is the coupling constant characterizing the Holstein-type interaction between the excitons and their local phonon environment.

We restrict our analysis to the single-excitation subspace. The corresponding basis states include: the exciton-photon ground state $|G, 0\rangle = |G\rangle \bigotimes_k |0_k\rangle$, the photon-dressed excitonic ground states

$$|G, 1_k\rangle = |G\rangle \bigotimes |1_k\rangle \bigotimes_{k' \neq k} |0_{k'}\rangle, \quad (5)$$

and the purely excitonic singly excited states with no photons

$$|E_n, 0\rangle = |E_n\rangle \bigotimes_k |0_k\rangle. \quad (6)$$

2.2 Polaritons

Polaritons arise from the super-position between exciton states and photonic excitation. In the reciprocal excitonic basis, for a given in-plane momentum k , the two polariton states can be expressed as linear combinations of their constituent exciton and photon states [13, 55]

$$|+_k\rangle = \sin \phi_k |E_k, 0\rangle + \cos \phi_k |G, 1_k\rangle, \quad (7a)$$

$$|-_k\rangle = \cos \phi_k |E_k, 0\rangle - \sin \phi_k |G, 1_k\rangle, \quad (7b)$$

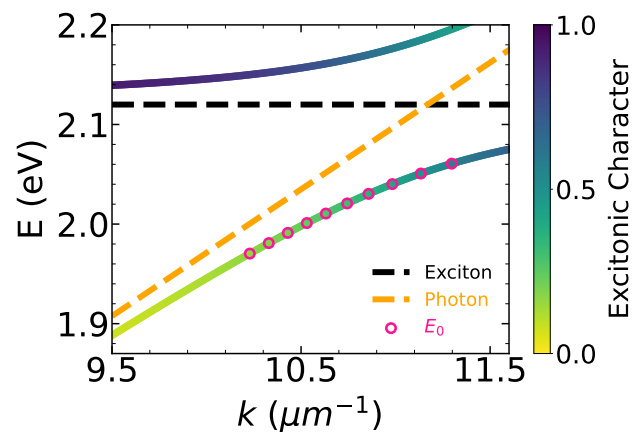


Fig. 1: Polariton dispersion relation showing the lower (LP) and upper (UP) polariton branches. The excitonic (black dashed) and photonic (orange dashed) dispersions are plotted for reference. The color scale indicates the Excitonic character ($|\alpha_{\text{ex}}|^2$) of the polaritonic states, ranging from photonic (yellow) to excitonic (dark violet). The pink open circles denote the location of the initial wavepacket in the LP branch for different simulations.

where $|+_k\rangle$ and $|-_k\rangle$ denote the upper polariton (UP) and lower polariton (LP) states, respectively.

The mixing angle ϕ_k , which quantifies the degree of hybridization between exciton and photon modes, is defined as [50, 55]:

$$\phi_k = \frac{1}{2} \tan^{-1} \left(\frac{2\sqrt{N}g_c}{\omega_k - \omega_0} \right), \quad \phi_k \in \left[0, \frac{\pi}{2} \right]. \quad (8)$$

$\sin \phi_k$ and $\cos \phi_k$ are called the Hopfield coefficients.

The state $|E_k, 0\rangle$ represents an exciton with in-plane momentum k and no photon:

$$|E_k, 0\rangle = \frac{1}{\sqrt{N}} \sum_n e^{iknL} |E_n, 0\rangle. \quad (9)$$

The energies of the polariton branches are given by [13]:

$$\omega_{\pm, k} = \frac{\omega_k + \omega_0}{2} \pm \frac{1}{2} \sqrt{(\omega_k - \omega_0)^2 + 4N g_c^2}. \quad (10)$$

In this model, polaritons are formed only when the wave vector of a photonic mode matches that of a collective excitonic mode. This condition is satisfied only at a discrete set of \mathcal{M} k -values corresponding to the allowed photon modes. The collection of these wave vectors is denoted as $\{k_p\}$. The polariton exhibits band-like transport characterized by the group velocity [15]

$$v_{g, \pm}(k) = d\omega_{\pm, k}/dk, \\ = \frac{1}{2} \left[1 \pm \frac{(\omega_k - \omega_0)}{\sqrt{(\omega_k - \omega_0)^2 + 4N g_c^2}} \right] \frac{d\omega_k}{dk}, \quad (11)$$

where the k -dependence of $\omega_{\pm, k}$ is carried by the bare photonic dispersion ω_k as given in Eq. 2. For, our BSW cavity with a linear dispersion, $\frac{d\omega_k}{dk}$ in Eq. 11 can be replaced by $\frac{c}{n_r} \text{sign}(k)$. Furthermore, by following the definition of the polaritonic states according to Eq. 7, the multiplicative prefactor in Eq. 11 corresponds precisely to the photonic component of the respective UP and LP states at that particular k , $|\alpha_{ph, \pm}(k)|^2$. Thus, Eq. 11 simplifies to

$$v_{g, \pm}(k) = \frac{c}{n_r} |\alpha_{ph, \pm}(k)|^2 \cdot \text{sign}(k). \quad (12)$$

Excitons with in-plane momenta k' that do not coincide with any existing photonic mode remain uncoupled from the light field and are referred to as *dark states*. These purely excitonic states can be written in the reciprocal basis as

$$|D_{k'}\rangle = \frac{1}{\sqrt{N}} \sum_n e^{ik'nL} |E_n, 0\rangle, \quad \forall k' \in \{k_D\}, \quad (13)$$

where $\{k_D\}$ denotes the set of wave vectors that do not host any photonic mode, even though corresponding collective excitonic modes exist. Unlike the bright states, dark states do not directly participate in light-matter hybridization but can mediate energy redistribution among polaritonic modes [21, 48, 49, 56–59]. It is important to note that the upper and lower polariton states ($\{|\pm_k\rangle\}$), together with the dark states ($\{|D_{k'}\rangle\}$), constitute the eigenstates of the polaritonic Hamiltonian, $\hat{H}_{\text{pl}} = \hat{H} - \hat{H}_{\text{ex-b}} - \hat{H}_{\text{b}}$ (see Section II in the Supplementary Material).

2.3 Computational Details

The system contains $N = 50001$ sites, with an inter-site spacing of $L = 100$ Å, and includes $\mathcal{M} = 4001$ photonic modes spanning the energy range $\hbar\omega_k \in [0.698, 3.898]$ eV. To describe the linear dispersion of the bare BSW photonic modes, together with the excitonic and polaritonic dispersions shown in Ref. 15, we use the following parameters: the excitation energy $\hbar\omega_0 = 2.12$ eV, the base photonic energy at the normal incidence (with $k = 0$) with $\hbar\omega_c = 0.698$ eV, the refractive index $n_r = 1.55$ and the Rabi splitting $\Omega_R = 2\hbar\sqrt{N}g_c = 134$ meV. For \mathcal{M} photonic modes, the wave vectors are discretized as $k_j = j \cdot \frac{2\pi}{NL}$, with $j \in \{-\frac{\mathcal{M}-1}{2}, -\frac{\mathcal{M}-3}{2}, \dots, 0, \dots, \frac{\mathcal{M}-3}{2}, \frac{\mathcal{M}-1}{2}\}$, where \mathcal{M} is an odd number.

To initialize the quantum dynamics at a chosen energy E_0 , the initial wavepacket is constructed as

a localized linear combination of all lower polaritonic (LP) states lying energetically close to E_0 . The coefficients of these individual LP states follow a Gaussian distribution centered at k_M , such that $\hbar\omega_{-,k_M} \approx E_0$. This initialization closely mirrors experimental conditions [13, 15, 47], where a highly focused pump pulse with narrow energy bandwidth and a momentum-selective probe pulse are employed. Further details on the preparation of the initial wavefunction are provided in Supplementary Material, Sec. III A.

We use the mean-field Ehrenfest dynamics approach to simulate polariton transport [13, 21, 46, 49, 60] in a lossless BSW cavity. In this scheme, the exciton-photon degrees of freedom (DOF) are treated quantum mechanically, while the phonon DOF are described classically. The phonon operators $\hat{q}_{n,v}$ and $\hat{p}_{n,v}$ are replaced by their classical counterparts $q_{n,v}$ and $p_{n,v}$ in H_b and H_{ex-b} . Each site is coupled to 20 phonon modes. To determine the phonon frequencies and coupling strengths [61], we employ a Drude–Lorentz spectral density [62, 63] with a reorganization energy $\lambda = 36$ meV and a characteristic frequency $\omega_b = 6$ meV. The initial positions and momenta of the phonons are sampled from a Wigner distribution at $T = 300$ K.

The state of the quantum subsystem is represented as

$$\begin{aligned} |\psi(t)\rangle &= \sum_{n=0}^{N-1} c_n(t)|E_n,0\rangle + \sum_{k \in \{k_P\}} c_k(t)|G,1_k\rangle \quad (14) \\ &\equiv |\psi_{ex}(t)\rangle \oplus |\psi_{ph}(t)\rangle, \end{aligned}$$

where $|E_n,0\rangle$ and $|G,1_k\rangle$ are defined in Eq. 6 and Eq. 5, respectively. This wavefunction is propagated by solving

$$i\hbar \frac{\partial}{\partial t} |\psi(t)\rangle = \hat{H}_Q(\mathbf{q}(t))|\psi(t)\rangle, \quad (15)$$

where $\hat{H}_Q = \hat{H} - \hat{H}_b$ is the quantum part of the Hamiltonian (that include excitonic and photonic DOF and exciton-phonon coupling). Chebyshev propagator [64] is employed to evolve the quantum subsystem. For a short time step δt , the position and momenta of the phonons are evolved according to the mean-field equations of motion $\dot{q}_{n,v}(t) = p_{n,v}(t)$, and

$$\begin{aligned} \dot{p}_{n,v}(t) &= -\langle\psi(t)|\frac{\partial\hat{H}}{\partial q_{n,v}}|\psi(t)\rangle, \quad (16) \\ &= -\omega_v^2 q_{n,v}(t) - \gamma_v \langle\psi(t)|\hat{\sigma}_n^\dagger \hat{\sigma}_n|\psi(t)\rangle. \end{aligned}$$

The classical phonon DOFs are integrated using the Velocity Verlet scheme. Further details regarding the system propagation, including the Chebyshev propaga-

tion technique, are discussed in sec. III C of the Supplementary Material. After performing quantum dynamical simulations under various initial conditions, the position of the polaritonic wavepacket was characterized by tracking the location of its tail, denoted as $\langle x \rangle_{ta}$. The precise definition and procedure for determining x_{ta} are provided in the Supplementary Material sec. IV B. The group velocity of the wavepacket was then evaluated as the time derivative of the tail position [13, 21, 49]

$$\tilde{v}_g = \frac{d\langle x \rangle_{ta}}{dt}. \quad (17)$$

Next, the mean-square displacement (MSD) of the wavepacket was computed as

$$MSD(t) = \sigma_t^2 - \sigma_0^2, \quad (18)$$

where the time-dependent variance σ_t^2 is defined by

$$\begin{aligned} \sigma_t^2 &= \langle X^2(t) \rangle - \langle X(t) \rangle^2 \quad (19) \\ &= \frac{1}{\sum_n P_n(t)} \sum_n x_n^2 P_n(t) - \left(\frac{1}{\sum_n P_n(t)} \sum_n x_n P_n(t) \right)^2. \end{aligned}$$

Here, $P_n(t)$ represents the total population contribution from LP and dark states at site x_n , given by [21]

$$P_n(t) = |\psi(x_n, t)|^2 \approx |\psi_{-}(x_n, t)|^2 + |\psi_D(x_n, t)|^2, \quad (20)$$

where $\psi_{-}(x_n, t)$ and $\psi_D(x_n, t)$ denote the spatial distributions of the lower polariton (LP) and dark-state components, respectively, as defined explicitly in the Supplementary Material, Sec. IV A. The temporal evolution of $MSD(t)$ was fitted to a power-law dependence, $MSD(t) \propto t^\beta$, to extract the transport exponent β . In regimes where $\beta = 1$, corresponding to diffusive transport, the MSD was further fitted as

$$MSD(t) = 2\mathcal{D}t \quad (21)$$

to determine the diffusion coefficient \mathcal{D} .

3 Results and Discussions

We investigate the polariton transport dynamics by initially exciting on the lower polariton (LP) branch, with different choices of k (as indicated by pink open circles in Fig. 1) by creating a LP wavepacket of a certain energy E_0 . The photonic fraction of these states decreases from 83% (for $E_{LP} = 1.97$ eV) to 44% (for

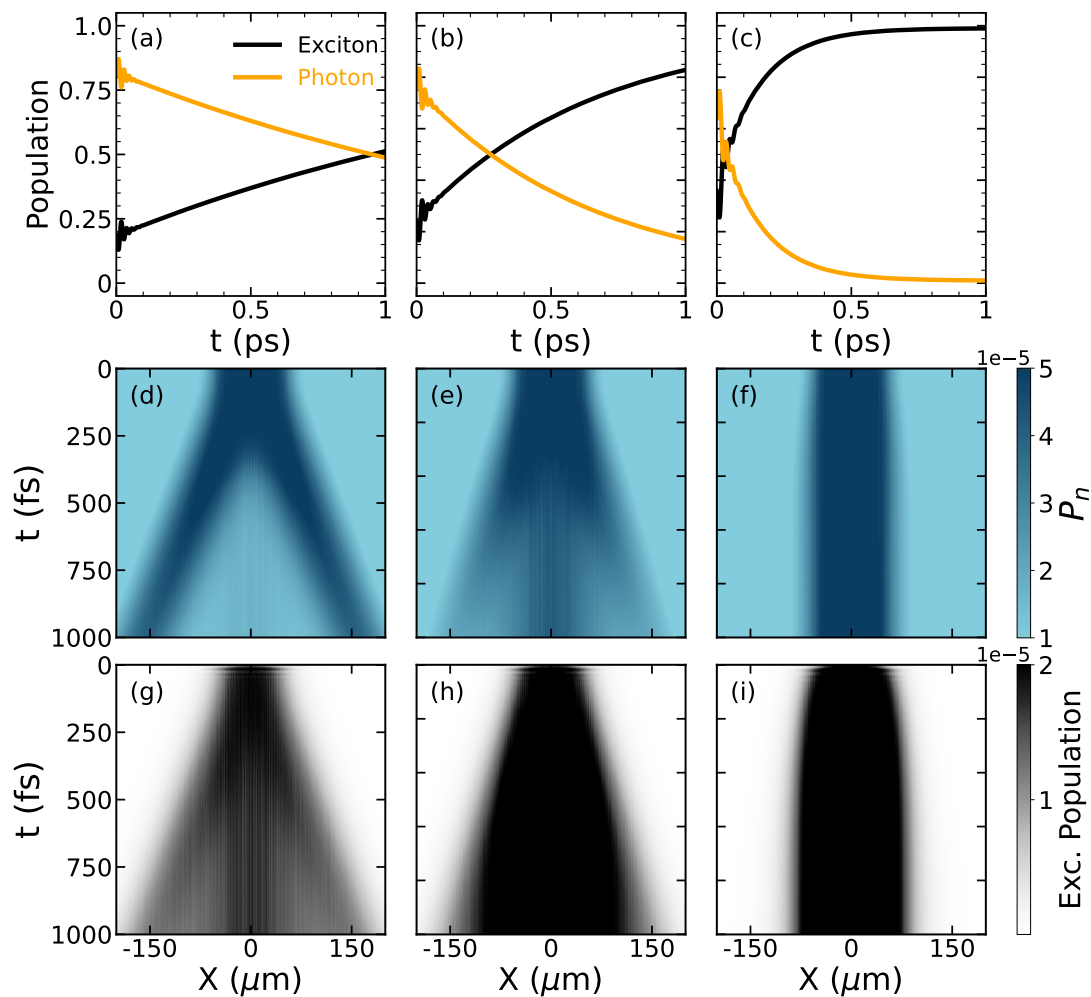


Fig. 2: Exciton–photon population dynamics and spatiotemporal evolution of wavepackets for three different initial excitation energies E_0 . Panels (a–c) display the time evolution of total excitonic and photonic populations for simulations initialized with $E_0 = 1.98$, 2.00, and 2.03 eV, respectively. Panels (d–f) and (g–i) show the corresponding spatiotemporal evolution of the lower-polariton+Dark and excitonic populations, respectively. While computing the site positions, the site index grid was shifted from $-\frac{N}{2}$ to $\frac{N}{2}$ such that the center of the simulation box lies at the origin. In these plots, the horizontal axis represents position along the molecular chain, the vertical axis represents propagation time, and the color scale indicates the population density.

$E_{LP} = 2.06$ eV), reflecting the increasing excitonic character with a higher energy in the case of negative detuning between light and matter.

Figure 2a–c shows the population dynamics of excitons and photons (c.f. Eq. 14) for three different initial energies, $E_0 = 1.98$ eV, 2.00 eV, and 2.03 eV, corresponding to excitonic fractions of 19%, 24%, and 36%, respectively. The initial fast oscillations of the populations between exciton (black) and photon (gold) are due to the light-matter coupling term (last term in Eq. 1) causing the Rabi oscillation, with the frequency corresponding to the Rabi splitting. The slower transfer between exciton and photon are mainly caused by exciton-phonon coupling term (\hat{H}_{ex-b} in Eq. 4), which

causes the population transfer from LP to the dark exciton manifold, and when projected to the exciton and photon basis, causing a slow transitions between these two subsystems. It is evident that as the excitonic character of the initial LP state increases, the transfer of population from the photonic to the excitonic DOF (dominate by the dark exciton component) becomes faster. This behavior arises from phonon-assisted scattering, which is more efficient for states with a larger excitonic component. The phonon scattering acts as a diabatic coupling between different polaritonic and dark states at various k , which are the eigenstates of the polaritonic Hamiltonian, \hat{H}_{pl} . Since the phonons couple directly to the excitonic part of the polaritonic

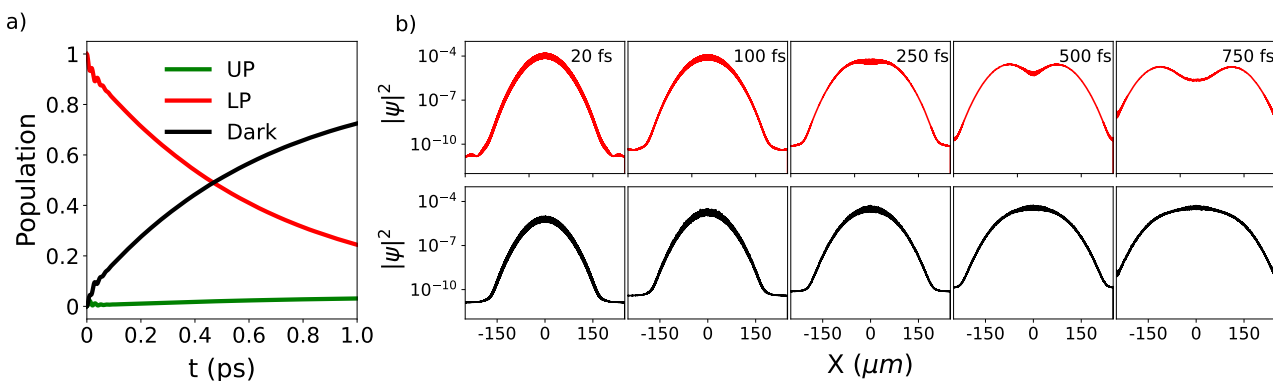


Fig. 3: (a) Temporal evolution of lower polariton (LP), upper polariton (UP), and dark-state populations for an initial energy of $E_0 = 2.00 \text{ eV}$. (b) Site-resolved population distributions at selected times. The top row shows contributions from LP states, while the bottom row displays contributions from dark states, both plotted on a logarithmic scale. Each column corresponds to a different time snapshot.

states, relaxation into purely excitonic dark states proceeds more rapidly when the LP wavepacket has a stronger excitonic character.

Fig. 2d–f presents the spatio-temporal evolution of the total LP and dark-state populations based on Eq. 20, and the purely excitonic population is shown in Fig. 2g–i presents the spatio-temporal evolution of exciton component based on $P^{(\text{ex})}_n = |\langle \psi_{\text{ex}}(t) | \psi_{\text{ex}}(t) \rangle|^2 = c * n c_n$ (c.f. Eq. 14). Moving from left to right, in both the second and third rows, one observes a progressive suppression of ballistic spreading of the wavepacket and a transition toward diffusive transport as the initial LP wavepacket becomes more excitonic. In all cases, the initial wave packet originates from the center of the simulation box and propagates toward both edges.

Comparing the spatial evolution of the combined LP+dark population with that of the purely excitonic population for a given E_0 , it becomes evident that the excitonic component propagates more slowly than the LP+dark wavepacket. Moreover, the excitonic population consistently retains a non-negligible density near the center of the simulation box—a feature that is largely absent in the more photonic LP wavepackets. Since dark states are purely excitonic, they propagate diffusively (in this model, they possess no net group velocity owing to the flat dispersion of the exciton branch), whereas LP states retain a ballistic component of transport depending on their photonic fraction. Consequently, the more photonic the LP state, the weaker the influence of phonon-assisted scattering and relaxation into dark states, leading to a more pronounced ballistic transport. Conversely, for LP states with larger excitonic character, phonon-assisted relax-

ation into dark states is more efficient, enhancing diffusive behavior.

The excitonic wavepacket thus arises from two contributions: a ballistic component from the LP states with finite group velocity, which is partly excitonic, and a diffusive component from the dark states that spread only slowly, but is purely excitonic. When the initial LP wavepacket is highly photonic, its weak coupling to dark states limits population transfer, making the LP contribution dominant. In contrast, for LP wavepackets with a larger excitonic character, phonon-mediated relaxation into dark states is faster, and these dark states—localized closer to the center—contribute most significantly to the excitonic population dynamics. The dark excitons also exhibit limited spatial propagation due to continuous population transfer from the fast-moving LP wavepacket, a mechanism where LP transport effectively “drags” the dark-state population, as discussed in our previous work [21]. This interplay explains why the excitonic wavepacket moves more slowly than the combined LP+dark population and why it consistently exhibits a non-negligible density near the center of the box.

These two competing propagation mechanisms—ballistic and diffusive—occur simultaneously, and the process by which the ballistic LP states dynamically “drag” the dark states is further illustrated in Fig. 3. Figure 3a shows the temporal evolution of the LP, UP, and dark-state populations for an initial energy of $E_0 = 2.00 \text{ eV}$. The dynamics are dominated by population transfer from the LP to the dark manifold, while the LP-to-UP transfer channel remains negligible, due to both the large energy separation between the LP and UP branches [65, 66], as well as



the weak phonon-mediated scattering efficiency of the predominantly photonic UP modes.

Figure 3b presents the site-resolved population distributions of LP and dark states at selected times, clearly highlighting the contrast in their transport behavior. The LP wavepacket splits into two symmetric components, corresponding to positive- and negative-momentum contributions, and rapidly propagates away from the center of the simulation box in a ballistic fashion. In contrast, the dark-state population exhibits purely diffusive broadening: its profile gradually widens over time, but the peak remains localized near the center. This behavior arises because the dark states do not possess intrinsic group velocity in our model; they gain population through phonon-assisted transfer from the propagating LPs and, once populated, remain nearly stationary on the timescale of observation. This mechanism explains the persistent high dark-state population around $X = 0$ and encapsulates the coexistence of ballistic polaritonic motion with diffusive dark-state spreading.

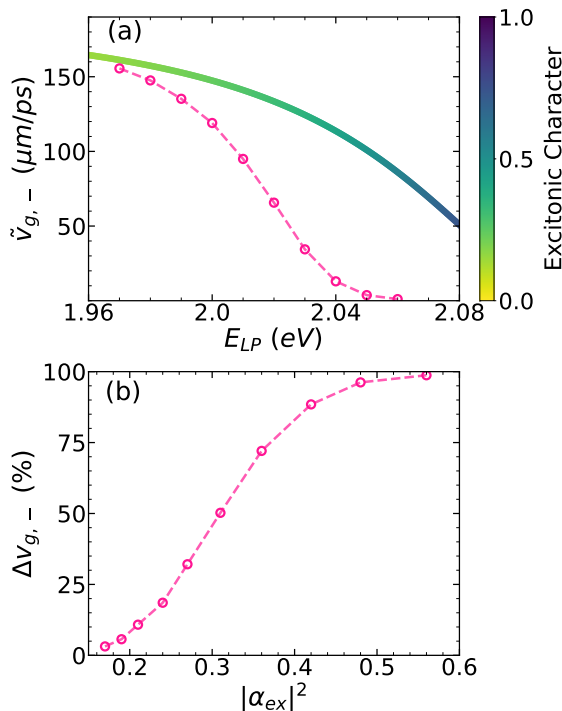


Fig. 4: (a) Group velocity as a function of lower polariton (LP) energy, E_{LP} . The solid line represents the theoretical group velocity, obtained as the slope of the LP dispersion ($\partial\omega_{-,k}/\partial k$), with the color scale indicating the excitonic fraction of the polariton. Pink open circles connected by a light pink dashed line denote the renormalized group velocities extracted from simulations at different E_{LP} . (b) The percentage renormalization of the group velocity plotted against the excitonic character of the initial wavepacket.

Figure 4a compares the simulated group velocities ($\tilde{v}_{g,-}$, pink open circles with dashed line) of LP wave packets at different energies with their corresponding theoretical values ($v_{g,-}$, solid line color-coded by excitonic fraction), calculated using Eq. 12. Across much of the LP branch, the theoretical group velocity approaches the speed of light, suggesting that—if preserved—such polaritons could enable ultrafast excitonic transport. However, the simulations reveal a systematic renormalization of $v_{g,-}$, even for highly photonic wave packets, with the effect becoming more pronounced as the excitonic character increases.

Figure 4(b) quantifies this effect by plotting the relative renormalization, $\Delta v_{g,-} = 1 - \tilde{v}_{g,-}/v_{g,-}$, as a function of excitonic fraction. The dependence exhibits a sigmoidal trend: $\Delta v_{g,-}$ initially shows negligible renormalization till around 20% excitonic character, then grows nearly linearly, and finally saturates near 100% once the excitonic character exceeds $\sim 50\%$. Thus, even wave packets with significant photonic content can have diffusive transport with vanishing group velocity in this regime, effectively behaving as excitonic packets.

This renormalization originates from phonon-assisted scattering between LP and dark states [49]. Since the scattering rate scales with the excitonic Hopfield coefficient of the LP state, larger excitonic fractions enhance the coupling and, consequently, the renormalization. Previous studies have shown that increasing phonon coupling strength—through higher reorganization energy λ , bath frequency ω_f , or temperature T —further amplifies this effect [21]. From a theoretical perspective, the phenomenon can be interpreted either as a phonon-induced renormalization of the polariton dispersion band via dark-state superexchange [49], or within the polaron–polariton framework using a Floquet formalism for phonon [60], where phonons generate additional sub-bands between LP and UP. Both viewpoints underscore that stronger excitonic character yields stronger LP–dark coupling, driving the observed suppression of group velocity. It is worth noting that previous studies have reported phonon-assisted enhancement of polariton group velocity, either with the presence of Peierls-type phonons [67] or when probing LP states with a very high excitonic character ($\sim 90\%$) [68]. While such scenarios highlight the diversity of phonon–polaritonic interactions and merit further investigation, they lie beyond the scope of the present work.

We next examine the spatial spreading of polaritonic wave packets by analyzing the time evolution

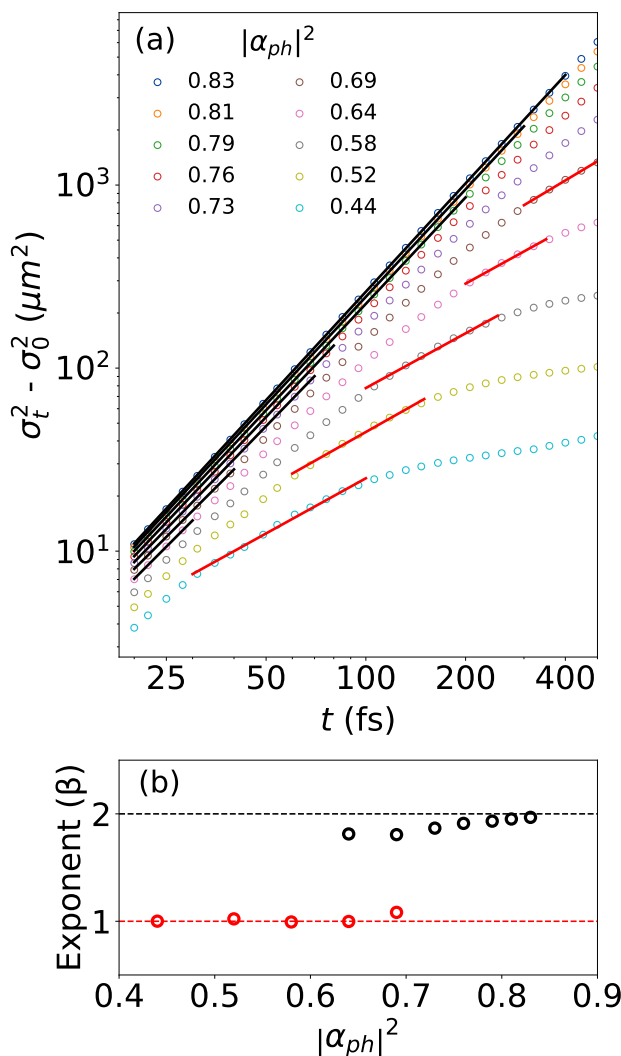


Fig. 5: Polaritonic transport dynamics for various initial excitation energies E_0 . (a) Time evolution of the mean squared displacement (MSD, $\sigma_t^2 - \sigma_0^2$) for $E_0 = 1.97\text{--}2.06\text{ eV}$. Each dataset represents an initial wavepacket at a given E_0 , colored by its photonic fraction. Black and red lines denote ballistic ($\text{MSD} \propto t^2$, $\beta = 2$) and diffusive ($\text{MSD} \propto t$, $\beta = 1$) regimes, respectively. (b) Extracted transport exponent β vs photonic fraction of the initial wavepacket. Polaritonic states with a high photonic contribution ($> 73\%$) remain ballistic, and those with a low photonic contribution ($< 58\%$) are diffusive, and intermediate ones show a ballistic–diffusive crossover.

of the mean square displacement (MSD), defined as $\sigma_t^2 - \sigma_0^2$, for wavepackets with various initial conditions. The colored open circles in Fig. 5a shows how MSD of the different LP wavepackets with a varying initial photon character as a function of time. Both axes are in log scale. We know that, for ballistic transport, which a purely photonic wave would undergo, the increase in MSD is proportional to t^2 , whereas for diffusive transport, which a purely excitonic wave would undergo, it is proportional to t . We have fitted the MSD of the wavepackets with t^β with $\beta = 1, 2$ in the time range of 20 fs to 500 fs and extracted the transport exponent β for the best fit. The fitted line is also shown in the figure. The region where MSD is proportional to t^2 are shown with a solid black line, whereas the region where MSD is proportional to t is shown with a solid red fitted line. It is evident that LP wavepackets with very high photonic character ($> 73\%$) show only ballistic transport ($\beta = 2$) for almost the whole range of the fit. Lowering the photon character of the wavepacket leads to ballistic transport at initial times of the simulation and then a transition to diffusive transport at later times. On the contrary, LP wavepackets with 40% or more excitonic character show only linear temporal evolution of MSD, always *i.e.* only diffusive transport, without any ballistic signature.

These trends are summarized in Fig. 5(b), which shows the extracted transport exponent β as a function of the initial photonic fraction. The systematic reduction of β with decreasing photonic character, together with the clear ballistic-to-diffusive crossover observed in several cases, highlights the crucial role of exciton–phonon scattering in suppressing ballistic propagation and driving the onset of diffusion. Notably, our theoretical results show excellent agreement with the experimental measurements reported in Fig. 4 of Ref. 15.

Finally, we evaluate the diffusion coefficient \mathcal{D} for those LP wavepackets that exhibit diffusive transport, either throughout or during a portion of the simulation time, according to the relation $\sigma_t^2 - \sigma_0^2 = 2\mathcal{D}t$. The extracted \mathcal{D} values are plotted in Fig. 6 as a function of the photonic character of the initial LP wavepacket. The red open circles represent the diffusion coefficients obtained by fitting the MSD in the time window where the transport exponent $\beta \approx 1$ [see Eq. 21], corresponding to the red solid line region in Fig. 5a. For comparison, the black open circles denote the previously calculated effective group velocities ($\tilde{v}_{g,-}$) for those cases exhibiting ballistic transport, while the solid black line

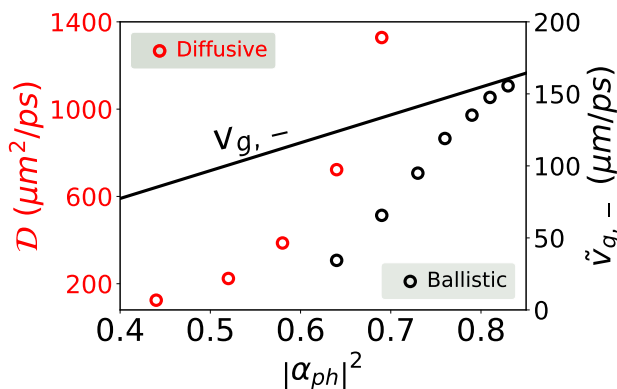


Fig. 6: Transport characteristics as a function of the photonic fraction ($|\alpha_{ph}|^2$) of the initial state. The red open circles correspond to the diffusion coefficient D (left axis) extracted from cases where MSD scales linearly with time ($\text{MSD} \propto t$), indicating diffusive transport. The black open circles represent the calculated group velocity \tilde{v}_g (right axis) obtained for cases exhibiting ballistic transport, where $\text{MSD} \propto t^2$. The solid black line denotes the theoretical group velocity v_g extracted from the polaritonic dispersion relation.

indicates the theoretical LP group velocity ($v_{g,-}$) derived from the slope of the LP dispersion.

As shown in Fig. 6, the diffusion coefficient D increases approximately quadratically with the photonic fraction of the initial LP wavepacket, reaching values as high as $\sim 1400 \mu\text{m}^2 \cdot \text{ps}^{-1}$ for highly photonic LPs. Even for LP wavepackets with a modest photonic content ($\approx 40\%$), D remains remarkably large ($\sim 30 \mu\text{m}^2 \cdot \text{ps}^{-1}$)—about four to eight orders of magnitude higher than typical excitonic diffusion coefficients in conventional semiconductors [69–72] in a range of 10^{-3} – $10^{-7} \mu\text{m}^2 \cdot \text{ps}^{-1}$). These results highlight the dramatic enhancement of transport efficiency enabled by polariton formation and the key role of photonic contribution in governing polariton mobility. Although the diffusion coefficients extracted from our simulations are approximately four times larger than the experimental values reported in Ref. 15, the results in Fig. 6 reproduce the same qualitative dependence (approximately quadratic) on $|\alpha_{ph}|^2$ observed experimentally (see Fig. 5 in Ref. 15). Moreover, the group velocities obtained from our simulations also show good qualitative agreement with the experimentally measured trends reported in Ref. 15.

4 Conclusion

In summary, our study establishes a comprehensive microscopic picture of phonon-influenced polariton transport in BSW cavity, revealing how the interplay between photonic and excitonic characters governs the transition of the transport dynamics from the ballistic regime to the diffusive regime. By initializing lower polariton (LP) wavepackets with systematically varied excitonic fractions, we demonstrate in Fig. 2 that phonon-mediated coupling to dark excitonic states leads to a rapid redistribution of population and a concomitant suppression of spatial spreading of the wavepacket, which in turn results in a lowering of group velocity (Fig. 4). The difference in propagation mechanism for LP and dark and how the LP “drags” the diffusively spreading dark states are apparent in Fig. 3. This manifests as a continuous crossover—from purely ballistic transport for highly photonic LPs to entirely diffusive motion for strongly excitonic ones, captured quantitatively by the transport exponent β in Fig. 5 and the renormalized group velocity $\tilde{v}_{g,-}$ highlighted in Fig. 4.

The diffusion coefficients extracted from the time-dependent mean square displacements reveal transport efficiencies up to eight orders of magnitude higher than those of bare excitons, underscoring the profound enhancement of energy mobility enabled by light–matter hybridization. At the same time, our results highlight that the mechanism facilitating long-range coherent transport—the photonic admixture—simultaneously reduces the excitonic participation that is crucial for device functionality. Thus, for polaritonic transport to be viable in functional optoelectronic or energy-harvesting devices, a fundamental challenge arises: to maintain ballistic propagation while preserving a sufficiently high excitonic fraction to ensure that a significant portion of the excitation is effectively transported.

The duality of ballistic and diffusive channels uncovered here provides a unifying framework for understanding phonon-assisted relaxation and transport in polaritonic systems. It suggests that future efforts toward practical polariton-based devices must navigate this delicate trade-off, potentially through tailored detuning, engineered phonon environments, or cavity designs that optimize both coherence and exciton participation. Our findings, therefore, lay the groundwork for the rational control of hybrid light–matter transport in solid-state and molecular platforms, bridging

the microscopic mechanisms of polariton–phonon interactions with macroscopic functionality.

Acknowledgements

This work was supported by the Department of Energy under Grant No. DE-SC0026212, the University of Rochester PumpPrimer II funding, as well as by the University of Rochester Office of the Vice President for Research, the School of Medicine and Dentistry, and Arts, Sciences & Engineering via the Center for Integrated Research Computing (CIRC). Computing resources were provided by the Center for Integrated Research Computing (CIRC) at the University of Rochester. P.H. appreciates valuable discussions and comments from Milan Delor and Tal Schwartz.

Data Availability

The data that support the plots within this paper and other findings of this study are available from the corresponding authors upon a reasonable request.

References

- [1] Raul Perea-Causin, Daniel Erkensten, Jamie M. Fitzgerald, Joshua J. P. Thompson, Roberto Rosati, Samuel Brem, and Ermin Malic. Exciton optics, dynamics, and transport in atomically thin semiconductors. 10(10): 100701. ISSN 2166-532X. doi:10.1063/5.0107665. URL <https://doi.org/10.1063/5.0107665>.
- [2] Tobias Brixner, Richard Hildner, Jürgen Köhler, Christoph Lambert, and Frank Würthner. Exciton transport in molecular aggregates – from natural antennas to synthetic chromophore systems. 7(16):1700236. ISSN 1614-6840. doi:10.1002/aenm.201700236. URL <https://onlinelibrary.wiley.com/doi/abs/10.1002/aenm.201700236>.
- [3] Drew B. Riley, Paul Meredith, and Ardalan Armin. Exciton diffusion in organic semiconductors: Precision and pitfalls. doi:10.1039/D4NR02467B. URL https://pubs.rsc.org/en/content/articlehtml/2024/nr/d4nr02467b?utm_source=chatgpt.com.
- [4] Can Gao, Zhagen Miao, Wallace W. H. Wong, Trevor A. Smith, Shih-Chun Lo, Wenping Hu, Ebinazar B. Namdas, and Huanli Dong. Management and utilization of triplet excitons in organic optoelectronic devices. ISSN 2667-3258. doi:10.1016/j.jfmre.2024.05.009. URL <https://www.sciencedirect.com/science/article/pii/S2667325824002188>.
- [5] Brian A. Gregg. Excitonic solar cells. 107(20):4688–4698. ISSN 1520-6106. doi:10.1021/jp022507x. URL <https://doi.org/10.1021/jp022507x>.
- [6] Thomas John Sheehan, Seryio Saris, and William A. Tisdale. Exciton transport in perovskite materials. 37(25):e2415757. ISSN 1521-4095. doi:10.1002/adma.202415757.
- [7] Christopher J. Bardeen. The structure and dynamics of molecular excitons. 65:127–148. ISSN 1545-1593. doi:10.1146/annurev-physchem-040513-103654.
- [8] Pengfei Qi, Yang Luo, Beibei Shi, Wei Li, Donglin Liu, Liheng Zheng, Zhixin Liu, Yanglong Hou, and Zheyu Fang. Phonon scattering and exciton localization: Molding exciton flux in two dimensional disorder energy landscape. 1(1): 6. ISSN 2662-8643. doi:10.1186/s43593-021-00006-8. URL <https://doi.org/10.1186/s43593-021-00006-8>.
- [9] S. M. Vlaming, V. A. Malyshev, A. Eisfeld, and J. Knoester. Subdiffusive exciton motion in systems with heavy-tailed disorder. 138(21):214316–1–214316–10. ISSN 0021-9606. doi:10.1063/1.4808155. URL <https://www.scopus.com/pages/publications/84879135126>.
- [10] Shaocong Hou, Mandeep Khatoniar, Kan Ding, Yue Qu, Alexander Napolov, Vinod M. Menon, and Stephen R. Forrest. Ultralong-range energy transport in a disordered organic semiconductor at room temperature via coherent exciton-polariton propagation. *Adv. Mater.*, 32, 7 2020. ISSN 15214095. doi:10.1002/adma.202002127.
- [11] Gal Sandik, Johannes Feist, Francisco J. García-Vidal, and Tal Schwartz. Cavity-enhanced energy transport in molecular systems. 24(3):344–355. ISSN 1476-1122, 1476-4660. doi:10.1038/s41563-024-01962-5. URL <https://www.nature.com/articles/s41563-024-01962-5>.
- [12] Anton Matthijs Berghuis, Ruth H Tichauer, Lianne MA de Jong, Ilia Sokolovskii, Ping Bai, Mohammad Ramezani, Shunsuke Murai, Gerrit Groenhof, and Jaime Gómez Rivas. Controlling exciton propagation in organic crystals through strong coupling to plasmonic nanoparticle arrays. *ACS photonics*, 9(7):2263–2272, 2022.
- [13] Ding Xu, Arkajit Mandal, James M Baxter, Shan-Wen Cheng, Inki Lee, Haowen Su, Song Liu, David R Reichman, and Milan Delor. Ultrafast imaging of polariton propagation and interactions. *Nat. Commun.*, 14(1):3881, 2023.
- [14] Shan Wen Cheng, Ding Xu, Haowen Su, James M. Baxter, Luke N. Holtzman, Kenji Watanabe, Takashi Taniguchi, James C. Hone, Katayun Barmak, and Milan Delor. Optical imaging of ultrafast phonon-polariton propagation through an excitonic sensor. *Nano Lett.*, 23:9936–9942, 11 2023. ISSN 15306992. doi:10.1021/acs.nanolett.3c02897.
- [15] Mukundakumar Balasubrahmanyam, Arie Simkhovich, Adina Golombek, Gal Sandik, Guy Ankonina, and Tal Schwartz. From enhanced diffusion to ultrafast ballistic motion of hybrid light-matter excitations. *Nat. Mater.*, 22(3):338–344, 2023.
- [16] Yuzhong Chen, Ying Shi, Yusong Gan, Haiyun Liu, Tengfei Li, Sanjib Ghosh, and Qihua Xiong. Unraveling the ultrafast coherent dynamics of exciton polariton propagation at room temperature. 23(18):8704–8711. ISSN 1530-6984, 1530-6992. doi:10.1021/acs.nanolett.3c02547. URL <https://pubs.acs.org/doi/10.1021/acs.nanolett.3c02547>.
- [17] Linrui Jin, Alexander D. Sample, Dewei Sun, Yao Gao, Shibin Deng, Ran Li, Letian Dou, Teri W. Odom, and

- Libai Huang. Enhanced two-dimensional exciton propagation via strong light–matter coupling with surface lattice plasmons. 10(6):1983–1991. ISSN 2330-4022, 2330-4022. doi:10.1021/acspolitronics.3c00466. URL <https://pubs.acs.org/doi/10.1021/acspolitronics.3c00466>.
- [18] Georgi Gary Rozenman, Katherine Akulov, Adina Golombek, and Tal Schwartz. Long-range transport of organic exciton-polaritons revealed by ultrafast microscopy. 5(1):105–110. ISSN 2330-4022, 2330-4022. doi:10.1021/acspolitronics.7b01332. URL <https://pubs.acs.org/doi/10.1021/acspolitronics.7b01332>.
- [19] Mark Steger. Long-range ballistic motion and coherent flow of long-lifetime polaritons. 88(23). doi:10.1103/PhysRevB.88.235314.
- [20] Ruth H Tichauer, Ilia Sokolovskii, and Gerrit Groenhof. Tuning the coherent propagation of organic exciton-polaritons through the cavity q-factor. *Adv. Sci.*, 10(33):2302650, 2023.
- [21] Benjamin X. K. Chng, M. Elious Mondal, Wenxiang Ying, and Pengfei Huo. Quantum dynamics simulations of exciton polariton transport. *Nano Lett.*, 25(4):1617–1622, 2025. doi:10.1021/acs.nanolett.4c05674. URL <https://doi.org/10.1021/acs.nanolett.4c05674>.
- [22] Ilia Tutunnikov, Md Qutubuddin, H. R. Sadeghpour, and Jianshu Cao. Characterization of polariton dynamics in a multimode cavity: Noise-enhanced ballistic expansion. URL <http://arxiv.org/abs/2410.11051>.
- [23] Federico Toffoletti and Elisabetta Collini. Coherent phenomena in exciton–polariton systems. 8(2):022002. ISSN 2515-7639. doi:10.1088/2515-7639/adcb6. URL <https://doi.org/10.1088/2515-7639/adcb6>.
- [24] Nguyen Ha My Dang, Simone Zanotti, Emmanuel Drouard, Céline Chevalier, Gaëlle Trippé-Allard, Emmanuelle Deleporte, Christian Seassal, Dario Gerace, and Hai Son Nguyen. Long-range ballistic propagation of 80% excitonic fraction polaritons in a perovskite metasurface at room temperature. 24(38):11839–11846. ISSN 1530-6984, 1530-6992. doi:10.1021/acs.nanolett.4c02696. URL <https://pubs.acs.org/doi/10.1021/acs.nanolett.4c02696>.
- [25] Ravindra Kumar Yadav, Matthew Otten, Weijia Wang, Christian L. Cortes, David J. Gosztola, Gary P. Wiederrecht, Stephen K. Gray, Teri W. Odom, and Jaydeep K. Basu. Strongly coupled exciton–surface lattice resonances engineer long-range energy propagation. 20(7):5043–5049. ISSN 1530-6984, 1530-6992. doi:10.1021/acs.nanolett.0c01236. URL <https://pubs.acs.org/doi/10.1021/acs.nanolett.0c01236>.
- [26] Yuriy Zakharko, Marcel Rother, Arko Graf, Bernd Hänilien, Maximilian Brohmann, Jörg Pezoldt, and Jana Zumseil. Radiative pumping and propagation of plexcitons in diffractive plasmonic crystals. 18(8):4927–4933. ISSN 1530-6984. doi:10.1021/acs.nanolett.8b01733. URL <https://doi.org/10.1021/acs.nanolett.8b01733>.
- [27] Giovanni Lerario, Dario Ballarini, Antonio Fieramosca, Alessandro Cannavale, Armando Genco, Federica Mangione, Salvatore Gambino, Lorenzo Dominici, Milena De Giorgi, Giuseppe Gigli, and Daniele Sanvitto. High-speed flow of interacting organic polaritons. 6(2):e16212–e16212. ISSN 2047-7538. doi:10.1038/lsa.2016.212. URL <https://www.nature.com/articles/lsa2016212>.
- [28] Ilia Sokolovskii, Yunyi Luo, and Gerrit Groenhof. Disentangling enhanced diffusion and ballistic motion of excitons coupled to Bloch surface waves with molecular dynamics simulations. 16(26):6719–6727. doi:10.1021/acs.jpclett.5c01391. URL <https://doi.org/10.1021/acs.jpclett.5c01391>.
- [29] Enes Suyabatmaz and Raphael F. Ribeiro. Vibrational polariton transport in disordered media. *J. Chem. Phys.*, 159(3):034701, 07 2023. doi:10.1063/5.0156008. URL <https://doi.org/10.1063/5.0156008>.
- [30] Saeed Rahamanian Koshkaki, Arshath Manjalingal, Logan Blackham, and Arkajit Mandal. Exciton-polariton dynamics in multilayered materials. URL <http://arxiv.org/abs/2502.12933>.
- [31] Arkajit Mandal, Ding Xu, Ankit Mahajan, Joonho Lee, Milan Delor, and David R. Reichman. Microscopic theory of multimode polariton dispersion in multilayered materials. 23(9):4082–4089. ISSN 1530-6984. doi:10.1021/acs.nanolett.3c01017. URL <https://doi.org/10.1021/acs.nanolett.3c01017>.
- [32] Arshath Manjalingal, Saeed Rahamanian Koshkaki, Logan Blackham, and Arkajit Mandal. Tilted material in an optical cavity: Light-matter moiré effect and coherent frequency conversion. URL <http://arxiv.org/abs/2508.11237>.
- [33] Bin Liu, Jason Lynch, Haonan Zhao, Ben R. Conran, Clifford McAleese, Deep Jariwala, and Stephen R. Forrest. Long-range propagation of exciton-polaritons in large-area 2d semiconductor monolayers. 17(15):14442–14448. ISSN 1936-0851, 1936-086X. doi:10.1021/acsnano.3c03485. URL <https://pubs.acs.org/doi/10.1021/acsnano.3c03485>.
- [34] Raj Pandya, Richard Y. S. Chen, Qifei Gu, Jooyoung Sung, Christoph Schnedermann, Oluwafemi S. Ojambati, Rohit Chikkaraddy, Jeffrey Gorman, Gianni Jacucci, Olimpia D. Onelli, Tom Willhammar, Duncan N. Johnstone, Sean M. Collins, Paul A. Midgley, Florian Auras, Tomi Baikie, Rahul Jayaprakash, Fabrice Mathevet, Richard Soucek, Matthew Du, Antonios M. Alvertis, Arjun Ashoka, Silvia Vignolini, David G. Lidzey, Jeremy J. Baumberg, Richard H. Friend, Thierry Barisien, Laurent Legrand, Alex W. Chin, Joel Yuen-Zhou, Semion K. Saikin, Philipp Kukura, Andrew J. Musser, and Akshay Rao. Microcavity-like exciton-polaritons can be the primary photoexcitation in bare organic semiconductors. 12(1):6519. ISSN 2041-1723. doi:10.1038/s41467-021-26617-w. URL <https://www.nature.com/articles/s41467-021-26617-w>.
- [35] J. Kasprzak, M. Richard, S. Kundermann, A. Baas, P. Jeambrun, J. M. J. Keeling, F. M. Marchetti, M. H. Szymańska, R. André, J. L. Staehli, V. Savona, P. B. Littlewood, B. Deveaud, and Le Si Dang. Bose-Einstein condensation of exciton polaritons. 443(7110):409–414. ISSN 1476-4687. doi:10.1038/nature05131.
- [36] R. Balili, V. Hartwell, D. Snoke, L. Pfeiffer, and K. West. Bose-Einstein condensation of microcavity polaritons in a trap. 316(5827):1007–1010. ISSN 1095-9203. doi:10.1126/science.1140990.
- [37] Alberto Amo, Jérôme Lefrère, Simon Pigeon, Claire Adrados, Cristiano Ciuti, Iacopo Carusotto, Romuald Houdré, Elisabeth Giacobino, and Alberto Bramati. Superfluidity of polaritons in semiconductor microcavities. 5(11):805–810. ISSN 1745-2481. doi:10.1038/nphys1364. URL <https://www.nature.com/articles/nphys1364>.

- [38] K. G. Lagoudakis, M. Wouters, M. Richard, A. Baas, I. Carusotto, R. André, Le Si Dang, and B. Deveaud-Plédran. Quantized vortices in an exciton–polariton condensate. 4(9):706–710. ISSN 1745-2481. doi:10.1038/nphys1051. URL <https://www.nature.com/articles/nphys1051>.
- [39] Anoop Thomas, Jino George, Atef Shalabney, Marian Dryzhakov, Sreejith J. Varma, Joseph Moran, Thibault Chervy, Xiaolan Zhong, Eloïse Devaux, Cyriaque Genet, James A. Hutchison, and Thomas W. Ebbesen. Ground-state chemical reactivity under vibrational coupling to the vacuum electromagnetic field. 55(38):11462–11466. ISSN 1521-3773. doi:10.1002/anie.201605504.
- [40] Robrecht M. A. Vergauwe, Anoop Thomas, Kalaivanan Nagarajan, Atef Shalabney, Jino George, Thibault Chervy, Marcus Seidel, Eloïse Devaux, Vladimir Torbeev, and Thomas W. Ebbesen. Modification of enzyme activity by vibrational strong coupling of water. 58(43):15324–15328. ISSN 1521-3773. doi:10.1002/anie.201908876. URL <https://onlinelibrary.wiley.com/doi/abs/10.1002/anie.201908876>.
- [41] Sebastian Montillo Vega, Wenxiang Ying, and Pengfei Huo. Theoretical insights into the resonant suppression effect in vibrational polariton chemistry. 147(23):19727–19737. ISSN 0002-7863, 1520-5126. doi:10.1021/jacs.5c03182. URL <https://pubs.acs.org/doi/10.1021/jacs.5c03182>.
- [42] Jialong Wang, Braden M. Weight, and Pengfei Huo. Investigating cavity quantum electrodynamics-enabled endo/exo-selectivities in a diels–alder reaction. 129(25):5458–5468. ISSN 1089-5639, 1520-5215. doi:10.1021/acs.jpca.5c01568. URL <https://pubs.acs.org/doi/10.1021/acs.jpca.5c01568>.
- [43] Gustavo J. R. Aroeira, Kyle T. Kairys, and Raphael F. Ribeiro. Coherent transient exciton transport in disordered polaritonic wires. *Nanophotonics*, 13(14):2553–2564, 2024. doi:doi:10.1515/nanoph-2023-0797. URL <https://doi.org/10.1515/nanoph-2023-0797>.
- [44] Ilia Sokolovskii, Ruth H Tichauer, Dmitry Morozov, Johannes Feist, and Gerrit Groenhof. Multi-scale molecular dynamics simulations of enhanced energy transfer in organic molecules under strong coupling. *Nat. Commun.*, 14(1):6613, 2023.
- [45] Gustavo J. R. Aroeira and Raphael F. Ribeiro. Static disorder-induced renormalization of polariton group velocity. 163(12):124120. ISSN 0021-9606. doi:10.1063/5.0288551. URL <https://doi.org/10.1063/5.0288551>.
- [46] Pritha Ghosh, Arshath Manjalingal, Sachith Wickramasinghe, Saeed Rahamanian Koshkaki, and Arkajit Mandal. Mean-field mixed quantum-classical approach for many-body quantum dynamics of exciton polaritons. 112(10):104319. ISSN 2469-9950, 2469-9969. doi:10.1103/m53p-sfc5. URL <https://link.aps.org/doi/10.1103/m53p-sfc5>.
- [47] Yongseok Hong, Ding Xu, and Milan Delor. Exciton delocalization suppresses polariton scattering. 0(0). ISSN 2451-9294, 2451-9308. doi:10.1016/j.chempr.2025.102759. URL [https://www.cell.com/chem/abstract/S2451-9294\(25\)00350-X](https://www.cell.com/chem/abstract/S2451-9294(25)00350-X).
- [48] Raj Pandya, Arjun Ashoka, Kyriacos Georgiou, Jooyoung Sung, Rahul Jayaprakash, Scott Renken, Lizhi Gai, Zhen Shen, Akshay Rao, and Andrew J. Musser. Tuning the coherent propagation of organic exciton-polaritons through dark state delocalization. *Adv. Sci.*, 9:2105569, 2022.
- [49] Wenxiang Ying, Benjamin X. K. Chng, Milan Delor, and Pengfei Huo. Microscopic theory of polariton group velocity renormalization. 16(1):6950. ISSN 2041-1723. doi:10.1038/s41467-025-62276-x. URL <https://www.nature.com/articles/s41467-025-62276-x>.
- [50] Arkajit Mandal, Michael AD Taylor, Braden M Weight, Eric R Koessler, Xinyang Li, and Pengfei Huo. Theoretical advances in polariton chemistry and molecular cavity quantum electrodynamics. *Chem. Rev.*, 123(16):9786–9879, 2023.
- [51] Michael A. D. Taylor, Arkajit Mandal, and Pengfei Huo. Light–matter interaction hamiltonians in cavity quantum electrodynamics. *Chem. Phys. Rev.*, 6(1):011305, 02 2025. doi:10.1063/5.0225932. URL <https://doi.org/10.1063/5.0225932>.
- [52] Liangyu Qiu, Arkajit Mandal, Ovishek Morshed, Mahilet T Meidenbauer, William Girten, Pengfei Huo, A Nickolas Vamivakas, and Todd D Krauss. Molecular polaritons generated from strong coupling between cdse nanplatelets and a dielectric optical cavity. *J. Phys. Chem. Lett.*, 12(20):5030–5038, 2021.
- [53] Ruth H. Tichauer, Johannes Feist, and Gerrit Groenhof. Multi-scale dynamics simulations of molecular polaritons: The effect of multiple cavity modes on polariton relaxation. 154(10):104112. ISSN 0021-9606. doi:10.1063/5.0037868. URL <https://doi.org/10.1063/5.0037868>.
- [54] Felipe Herrera and Frank C Spano. Theory of nanoscale organic cavities: The essential role of vibration-photon dressed states. *ACS photonics*, 5(1):65–79, 2018.
- [55] Hui Deng, Hartmut Haug, and Yoshihisa Yamamoto. Exciton-polariton bose-einstein condensation. *Rev. Mod. Phys.*, 82:1489–1537, May 2010. doi:10.1103/RevModPhys.82.1489. URL <https://link.aps.org/doi/10.1103/RevModPhys.82.1489>.
- [56] Carlos Gonzalez-Ballester. Uncoupled dark states can inherit polaritonic properties. 117(15). doi:10.1103/PhysRevLett.117.156402.
- [57] Eric Davidsson and Markus Kowalewski. The role of dephasing for dark state coupling in a molecular tavis-cummings model. 159(4):044306. ISSN 1089-7690. doi:10.1063/5.0155302.
- [58] Lucas Borges, Thomas Schnappinger, and Markus Kowalewski. Impact of dark polariton states on collective strong light-matter coupling in molecules. 16(31):7807–7815. ISSN 1948-7185. doi:10.1021/acs.jpcllett.5c01480.
- [59] Woo Je Chang, Hongfei Zeng, Connor K. Terry Weatherly, Justin Provazza, Pufan Liu, Emily A. Weiss, Nathaniel P. Stern, and Roel Tempelaar. Dark state concentration dependent emission and dynamics of cdse nanplatelet exciton-polaritons. ISSN 1936-086X. doi:10.1021/acsnano.4c03545.
- [60] Logan Blackham, Arshath Manjalingal, Saeed R Koshkaki, and Arkajit Mandal. Microscopic theory of polaron-polariton dispersion and propagation. *arXiv preprint arXiv:2501.16622*, 2025.
- [61] Peter L. Walters, Thomas C. Allen, and Nancy Makri. Direct determination of discrete harmonic bath parameters from molecular dynamics simulations. 38(2):110–115. ISSN 1096-987X. doi:10.1002/jcc.24527. URL <https://onlinelibrary.wiley.com/doi/abs/10.1002/jcc.24527>.



- [62] A.O Caldeira and A.J Leggett. Quantum tunnelling in a dissipative system. *Ann. Phys.*, 149(2):374–456, 1983. ISSN 0003-4916. doi:[https://doi.org/10.1016/0003-4916\(83\)90202-6](https://doi.org/10.1016/0003-4916(83)90202-6). URL <https://www.sciencedirect.com/science/article/pii/0003491683902026>.
- [63] A. Nitzan. *Chemical Dynamics in Condensed Phases*. Oxford, New York, 2006.
- [64] M. Elious Mondal, A. Nickolas Vamivakas, Steven T. Cundiff, Todd D. Krauss, and Pengfei Huo. Polariton spectra under the collective coupling regime. i. efficient simulation of linear spectra and quantum dynamics. *The Journal of Chemical Physics*, 162(1):014114, 2025. doi:10.1063/5.0243535. URL <https://doi.org/10.1063/5.0243535>.
- [65] Benjamin X. K. Chng, Wenxiang Ying, Yifan Lai, A. Nickolas Vamivakas, Steven T. Cundiff, Todd D. Krauss, and Pengfei Huo. Mechanism of molecular polariton decoherence in the collective light-matter couplings regime. *J. Phys. Chem. Lett.*, 15(47):11773–11783, 2024. doi:10.1021/acs.jpclett.4c03049. URL <https://doi.org/10.1021/acs.jpclett.4c03049>.
- [66] Yifan Lai, Wenxiang Ying, and Pengfei Huo. Non-equilibrium rate theory for polariton relaxation dynamics. *J. Chem. Phys.*, 161(10):104109, 09 2024. doi:10.1063/5.0231396. URL <https://doi.org/10.1063/5.0231396>.
- [67] Guangming Liu and Hsing-Ta Chen. Dissecting exciton-polariton transport in organic molecular crystals: Emerging conductivity assisted by intermolecular vibrational coupling. URL <http://arxiv.org/abs/2505.21888>.
- [68] Niclas Krupp, Gerrit Groenhof, and Oriol Vendrell. Quantum dynamics simulation of exciton-polariton transport. 16(1):5431. ISSN 2041-1723. doi:10.1038/s41467-025-61298-9. URL <https://www.nature.com/articles/s41467-025-61298-9>.
- [69] Naomi S. Ginsberg and William A. Tisdale. Spatially resolved photogenerated exciton and charge transport in emerging semiconductors. 71:1–30. ISSN 0066-426X, 1545-1593. doi:10.1146/annurev-physchem-052516-050703. URL <https://www.annualreviews.org/content/journals/10.1146/annurev-physchem-052516-050703>.
- [70] Gleb M. Akselrod, Parag B. Deotare, Nicholas J. Thompson, Jiye Lee, William A. Tisdale, Marc A. Baldo, Vinod M. Menon, and Vladimir Bulović. Visualization of exciton transport in ordered and disordered molecular solids. 5(1):3646. ISSN 2041-1723. doi:10.1038/ncomms4646. URL <https://www.nature.com/articles/ncomms4646>.
- [71] Tong Zhu, Yan Wan, and Libai Huang. Direct imaging of frenkel exciton transport by ultrafast microscopy. 50(7):1725–1733. ISSN 1520-4898. doi:10.1021/acs.accounts.7b00155.
- [72] Anton Matthijs Berghuis, T. V. Raziman, Alexei Halpin, Shaojun Wang, Alberto G. Curto, and Jaime Gómez Rivas. Effective negative diffusion of singlet excitons in organic semiconductors. 12(4):1360–1366. doi:10.1021/acs.jpclett.0c03171. URL <https://doi.org/10.1021/acs.jpclett.0c03171>.